Efficient Quantification of Fluid Flow Parameter Sensitivity Using Reduced-Order Modeling

Harley Hanes[*]
North Carolina State University, Raleigh, NC 27695

Michael W. Lee[†]
NASA Langley Research Center, Hampton, VA 23681

Ralph C. Smith[‡]
North Carolina State University, Raleigh, NC 27695

Sensitivity analysis for computational fluid dynamics (CFD) simulations is often required for many applications but complicated by the computational cost of simulation codes. For many applications, the computational cost of quantifying the simulation's sensitivity to physical parameters (e.g., body surface roughness) and hyperparameters (e.g., subiteration convergence criterion) can be intractable for even a single simulation. Reduced-order modeling significantly reduces the computational cost of simulating fluid flows by solving on a reduced solution space informed by prior simulation data. In this work, fluid reduced-order models using boundary penalties are developed and utilized to quantify flow sensitivity to physical parameters, boundary conditions, and model hyperparameters. The proposed reduced-order modeling approach allows sensitivity analysis and uncertainty quantification of boundary conditions and enables more informed CFD frameworks.

Nomenclature

a	=	proper orthogonal decomposition coefficient
b	=	boundary penalty term
B	=	boundary penalty term integrated matrix
$\mathbf{C}$	=	reduced-order model constant vector
d	=	Morris screening function sensitivity
E_k	=	integrated kinetic energy
ℓ	=	relative length of the maximum function axis
L	=	reduced-order model linear matrix

[*]Doctoral Candidate, Department of Mathematics, North Carolina State University.
[†]Research Aerospace Engineer, Configuration Aerodynamics Branch, NASA Langley Research Center, AIAA Member.
[‡]Distinguished University Professor, Department of Mathematics, North Carolina State University.

N	=	Number of Morris screening parameter samples
M	=	Number of POD modes used
$\mathbf{M}$	=	reduced-order model mass matrix
P	=	fluid static pressure
$\mathbf{P}$	=	reduced-order model pressure vector
Q	=	reduced-order model nonlinear matrix
$\mathbb{R}$	=	the real number space
Re	=	Reynolds number
S	=	physical system dimension
t	=	time
u	=	fluid velocity vector
$\bar{v}$	=	velocity magnitude
V	=	integrated vorticity
W	=	quadrature weights
$\mathbf{x}$	=	position vector of dimension S
α	=	lid cavity velocity boundary coefficient
δ	=	Dirac delta distribution
Δ	=	parametric step size
Γ	=	fluid domain boundary
θ	=	parameter sample
φ	=	basis function orientation
ϕ	=	proper orthogonal decomposition mode
Φ	=	complete modal matrix
μ	=	Morris sensitivity mean
μ^*	=	Morris sensitivity absolute mean
σ	=	Morris sensitivity standard deviation
κ	=	boundary penalty strength
ξ	=	mean-reduction basis function location
ω	=	vorticity
Ω	=	fluid domain
BP-POD-ROM	=	Boundary-Penalized POD-based ROM
CFD	=	Computational Fluid Dynamics

DNS   =   Direct Numerical Simulation

POD   =   Proper Orthogonal Decomposition

ROM   =   Reduced-order Model

I. Background and Motivation

COMPUTATIONAL fluid dynamics (CFD) is employed in many facets of aerospace engineering. The chaotic nature of many fluid flows mandates the use of computational methods to quickly quantify flow dynamics and supplement the information provided by physical experiments. However, for methods quantifying the variation of solutions on applied configuration-scale problems, particularly sensitivity analysis, even cheaper computational formulations such as Reynolds-averaged Navier-Stokes (RANS) are often too computationally expensive. For this reason, the development of reduced-ordered model (ROM) methods, which can adequately quantify solution changes caused by parameter variations at a significantly reduced computational cost, is a critical goal for improving CFD accuracy and applicability.

Sensitivity analysis quantifies how variability in model outputs, such as velocity or vorticity, is influenced by variability in model parameters, such as Reynolds number. In aerospace applications, sensitivity analysis has been employed to quantify the influence of model parameters for atmospheric entry [1–3], commercial aircraft design [4], and shape optimization [5]. Parameters with high sensitivity may require more accurate measurement or can be adjusted to improve performance, whereas parameters with low sensitivity may be fixed for model reduction without loss in model fidelity [6]. An important classification of sensitivity analysis methods is whether they are local – measuring sensitivity at a single set of parameter values – or global – quantifying sensitivity over an assumed distribution of parameter values. Local methods are more computationally efficient but cannot determine dependencies over the admissible parameter space [6]. In this work, we implement Morris screening, a global sensitivity analysis method, and assess its strengths and weaknesses on a lid-driven cavity test problem [7]. Morris screening is well-established method in sensitivity analysis of physical models that globally averages local sensitivities to permit quantification of sensitivity across parameter distributions without the high computational costs of other global methods such as Sobol analysis [8–10].

Sensitivity analysis methods can require thousands of model evaluations, which can render them intractable for implementation for high-fidelity computational models. However, lower-cost (ROMs) enable sufficiently fast data throughput and sufficient fidelity for accurate sensitivity analysis. A common method is proper orthogonal decomposition (POD)-based Galerkin reduced-order modeling (POD-ROM), which projects the governing equations onto a spanning mode space, thus reducing them to a system of temporal ordinary differential equations [11]. However, many design-relevant parameters are not explicitly expressed in POD-ROMs, which limits their use for sensitivity analysis.

In this work, we employ a boundary penalty method with a standard POD-ROM. Boundary penalties have an

3

established use in POD-ROMs quantifying boundary information to improve stability [12, 13]. Boundary penalties also enable explicit control of the ROM-simulated boundary conditions, thereby facilitating sensitivity analysis. Within conventional wind tunnel- and CFD-centric design cycles, the significance of unavoidable differences in both far- and near-field boundary conditions are often difficult to study directly. This ROM framework addresses that limitation. Gust responses [14] and vehicle surface roughness [15] are just two types of parametric and hyperparametric sensitivities that can be quantified using such a boundary penalty method within the POD-ROM.

We test this methodology using boundary penalties to compute the sensitivity of POD-ROM solutions to boundary conditions for a 2D regularized lid-driven cavity. We compute the sensitivity of velocity, vorticity, and kinetic energy when varying boundary conditions between regularized and unregularized. To the authors' knowledge, this is the first investigation of an incompressible lid-driven cavity flow's sensitivity to boundary conditions. Studies investigating intermediate boundary conditions in viscoelastic lid-driven cavities exist, but we do not derive expected results from this study due to the large differences in flow characteristics between turbulent incompressible flows and low-Reynolds number viscous flows [16]. Therefore, we compare our results to studies of streamline characteristics of regularized and unregularized lid-driven cavities at different Reynolds numbers [17, 18].

We summarize Morris screening sensitivity analysis in Section II.A and derive the incompressible formulation of the proper orthogonal decomposition-based reduced-order model with boundary penalty, BP-POD-ROM, in Section II.B. We then provide a brief description of a 2-D regularized lid-driven cavity model selected to test the method in Section II.C. Finally, we present Morris screening results on the test case, exploring the sensitivity of physical parameters including Reynolds number and boundary condition compared to model parameters of penalty strength and the mean decomposition in Section III. We intend as future work testing of our method on recirculating tank models with a larger parameter space to further determine accuracy for sensitivity analysis and uncertainty quantification.

II. Methodology

A. Morris Screening

We employ Morris screening to compute the sensitivity of a BP-POD-ROM to model parameters. Morris screening is a one-at-a-time (OAT) quasiglobal sensitivity analysis method, which approximates the local derivatives at parameter values sampled from an assumed distribution [7]. Morris screening can be used to approximate derivative-based global sensitivity measures (DGSM), which define sensitivity to be the partial derivative of model outputs to model inputs, integrated over parameter distributions [6, 19]. Similar to the common alternative approach of Sobol analysis, Morris screening indices may be used to identify non-influential parameters and parameters with nonlinear or coupled effects [6, 20]. However, Morris screening is less computationally expensive, less impacted by error in assumed parameter distributions, and does not require that parameters are independently distributed [6].

4

Given a set of N parameter samples $\{\theta^j\}_{j=1}^N$ and a step-size Δ, Morris screening first computes finite-difference approximations of local sensitivity

$$d_i^j = \frac{f(\xi, \theta^j + \Delta e_i) - f(\xi, \theta^j)}{\Delta} \tag{1}$$

where f is an arbitrary function defined at basis function location ξ and parameter point θ, and e_i is the unit vector for parameter i. Morris screening then computes the sensitivity indices for absolute mean μ_i^* and standard deviation σ_i. Formulae for these indices are

$$\mu_i^* = \frac{1}{N} \sum_{j=1}^N |d_i^j|, \quad \sigma_i = \sqrt{\frac{1}{N-1} \sum_{j=1}^N (d_i^j - \mu_i)^2} \tag{2}$$

The absolute mean μ_i^* quantifies the sensitivity magnitude, where parameters with larger μ_i^* have greater sensitivity over the sampling region [10]. The absolute mean can be used to identify non-influential parameters which can be fixed for future calibration and uncertainty quantification. The standard deviation σ_i quantifies the sensitivity variation and identifies parameters that may have nonlinear or coupled effects on a quantity [10]. Additionally, parameters with large σ_i compared to μ_i^* may be highly sensitive but only for a small portion of their distribution.

Selection of Δ determines how finely the parameter space is searched around each parameter sample θ^j. Very small values provide a finite-difference derivative approximation whereas large values instead quantify large-scale function variations [6]. We normalize all parameter ranges to $[0, 1]$ before implementing Morris screening for nondimensional scaling of Δ, assume parameters are uniformly distributed to $[0, 1]$, and use $\Delta = 10^{-4}$. We sample parameters with quasi-random Sobol samples, which increases the accuracy of Morris screening compared to random sampling [21].

B. POD-ROM with Boundary Penalty

We develop a proper orthogonal decomposition-based reduced-order model with boundary penalty, BP-POD-ROM, by introducing a penalty term enforcing the boundary condition into a standard reduced-order model. Boundary-penalties have a well established use in POD-ROMs improving stability of solutions [12, 22]. We follow the POD-ROM derivation outlined in Ref. [23], using the penalty formulation found in Ref. [12].

We begin with a 2-dimensional incompressible Navier-Stokes system with Dirichlet boundary conditions

$$\begin{cases} \partial_t u^i + u^j \nabla^j u^i = -\nabla^i P + \frac{1}{Re} \nabla^2 u^i & \boldsymbol{x} \in \Omega = [0, 1]^2 \\ u = u_\Gamma & x \in \Gamma = \partial\Omega \end{cases} \tag{3}$$

where $u^i(\boldsymbol{x}, t)$ is the velocity in the ith direction and P is the pressure. To enforce the boundary condition Γ, we define the boundary penalty term

$$b_\Gamma^i(\boldsymbol{x}, t; \kappa) = \kappa \delta_\Gamma(\boldsymbol{x}) \left(u_\Gamma^i - u^i \right) \tag{4}$$

where $\delta_\Gamma(\boldsymbol{x})$ is the Dirac delta distribution such that,

$$\int_\Omega \delta_\Gamma(\boldsymbol{x})u(\boldsymbol{x})dx = \int_\Gamma u(\boldsymbol{x})dx$$

Here $\kappa > 0$ determines the the strength of the penalty [12]. We then add the penalty to the Navier-Stokes equations and construct the penalized system

$$\partial_t u^i + u^j \nabla^j u^i = -\nabla^i P + \frac{1}{Re}\nabla^2 u^i + b^i_\Gamma(\boldsymbol{x}, t; \kappa) \qquad \boldsymbol{x} \in \Omega \cup \Gamma \tag{5}$$

To compute the POD-ROM of the penalized system, we decompose the velocity by assuming $u^i = u^i_0 + u^i_d$, where $u^i_0(\boldsymbol{x})$ is a temporally constant field, often set as the temporal mean of the flowfield, and $u^i_d(\boldsymbol{x}, t)$ is the remaining portions of the flow with homogeneous Dirichlet boundary conditions. We note that POD-ROM solutions can deviate from the boundary conditions since explicit enforcement of the boundary is not included in POD formulation which boundary penalties can solve in many circumstances [12, 13]. By separating u^i into its two subcomponents, we expand Equation (5) into

$$\partial_t u^i_d = -u^j_0 \nabla^j u^i_0 - u^j_0 \nabla^j u^i_d - u^j_d \nabla^j u^i_0 - u^j_d \nabla^j u^i_d - \nabla^i P + \frac{1}{Re}(\nabla^2 u^i_0 + \nabla^2 u^i_d) + \kappa\delta(\boldsymbol{x})\left(u^i_\Gamma - (u^i_0 + u^i_d)\right) \tag{6}$$

We then expand u^i_d into a linear modal sum, which separates the spatial and the temporal velocity components:

$$u^i_d(\boldsymbol{x}, t) = a_n(t)\phi^i_n(\boldsymbol{x}) \tag{7}$$

Using the modal decomposition, we can expand Equation (6) into M – the number of POD modes – differential equations for modal coefficients. This yields the equation

$$\phi^i_n \partial_t a_n = -a_n a_m \phi^j_n \nabla^j \phi^i_m - \nabla^i P - (u^j_0 \nabla^j \phi^i_n + \phi^j_n \nabla^j u^i_0 - \frac{1}{Re}\nabla^2 \phi^i_n)a_n - u^j_0 \nabla^j u^i_0 + \frac{1}{Re}\nabla^2 u^i_0 + \kappa\delta(\mathbf{x})\left(u^i_\Gamma - (a_n \phi^i_n + u^i_0)\right) \tag{8}$$

Multiplying Equation (8) by the modal basis $\{\phi_m\}^M_{m=1}$ and integrating yields the Galerkin weak form for Navier-Stokes. The resulting temporal differential equations for $\alpha_n(t)$ can be expressed by the following system

$$\mathbf{M}\dot{\mathbf{a}} = \mathbf{a}^T[Q]\mathbf{a} + \left(\mathbf{L}^0 + \frac{1}{Re}\mathbf{L}^{Re} + \kappa\mathbf{B}\right)\mathbf{a} + \mathbf{P} + \mathbf{C}^0 + \frac{1}{Re}\mathbf{C}^{\mathbf{Re}} + \kappa\mathbf{B}^0 \tag{9}$$

For a flow with a set of spatial discretization points on the boundary Z, modal matrix Φ, and boundary quadrature

weights W, the formulae for the boundary penalty POD-ROM matrices are

$$B_{kn} = -(\phi_k^i, \ \phi_n^i)_{L^2(\Gamma_1)} = -\int_\Gamma \phi_k^x \phi_n^x + \phi_k^y \phi_n^y dS = \sum_{(x,y)\in Z} \sum_{i=1}^{2} \Phi_{xyk}^i \Phi_{xyn}^i W_{xy} \tag{10}$$

$$B_k^0 = (\phi_k^i, \ u_\Gamma^i - u_0^i)_{L^2(\Gamma)} = \int_{\Gamma_1} \phi_k^x \left(u_\Gamma^x - u_0^x\right) + \phi_k^y \left(u_\Gamma^y - u_0^y\right) dS = \sum_{(x,y)\in Z} \sum_{i=1}^{2} \Phi_{xyk}^i \left(u_{\Gamma,xy}^i - u_{0,xy}^i\right) W_{xy} \tag{11}$$

Formulae for $\mathbf{M}$, $[Q]$, $\mathbf{L}^0$, $\mathbf{L}^{Re}$, $\mathbf{C}^0$, and $\mathbf{C}^{\mathbf{Re}}$ as derived in [23] are provided in Appendix A. We also note that $\mathbf{P} \equiv 0$ in incompressible POD-ROMs due to the divergence-free characteristic of those POD modes, but that this property is not guaranteed with the addition of the boundary penalty terms [12]. However, the pressure gradient in the lid-driven cavity test problem is near-zero so we assume it to be zero for the rest of this analysis [17].

C. Lid-Driven Cavity Test Case

To verify the implementation of the BP-POD-ROM, we utilize the incompressible 2-D regularized lid-driven cavity. This flow regime has been studied exhaustively, including investigation of how different Reynolds numbers and boundary conditions influence flow solutions [24]. Lid-driven cavity problems are classified as regularized or unregularized according to their boundary condition. All 2-D lid-driven cavities are rectangular domains with homogeneous Dirichlet boundary conditions on three walls with a nonhomogeneous Dirichlet boundary condition parallel to the fourth wall. In the unregularized case, the condition is constant along the nonhomogenous boundary, causing a discontinuity at the corners. In the regularized case, it is a smooth nonnegative definite function that converges to zero at both boundary edges in both the velocity and its gradient, eliminating the discontinuity [25]. Both cases have similar dynamics and bifurcations but the unregularized lid-driven cavity experiences them at lower Reynolds numbers [17, 24]. We nondimensionalize spatial units with respect to a length scale equal to half the width of the cavity and time units with respect to a flow velocity equal to the maximum velocity of the boundary condition.

For snapshot data, we use regularized lid-driven cavity simulations computed via direct numerical simulations (DNS) at $Re = 17,000$ and $Re = 25,000$ and at a discretization of 256×256 points [17, 26]. For the smaller Reynolds number, the flow exhibits quasi-periodic dynamics; at the higher Reynolds number, the flow is fully aperiodic and formally chaotic. We form a snapshot matrix using the first 150 time-steps with a statistically stationary time history and reduce them to 100 POD modes, which contain over 99.99% of the snapshot matrix mean fluctuating kinetic energy for both Reynolds numbers.

We define the parameterized boundary condition as

$$u_\Gamma(x; \alpha) = |(1 - x)(1 + x)|^{2\alpha} \tag{12}$$

We note that $u_\Gamma(x, 1)$ is equivalent to the regularized boundary, $u_\Gamma(x, 0)$ is equivalent to the unregularized boundary. Furthermore, $u_\Gamma(x; \alpha)$ is well-defined for $x \in [0, 1]$ so the boundary condition is suitable for continuous perturbation of α in Morris screening.

To test the sensitivity of POD-ROM solutions to the mean reduction snapshot u_0^i, we employed an artificial snapshot computed from a stream function created by summing weighted Gaussian functions

$$f_i(\boldsymbol{x}; \boldsymbol{\xi}_i, \ell_i, \varphi_i) = \bar{v}_i e^{-(\boldsymbol{x}-\boldsymbol{\xi})^T \Sigma (\boldsymbol{x}-\boldsymbol{\xi})}, \qquad \Sigma = 20 \begin{bmatrix} \ell_i \sin(\varphi_i) & -\ell_i \cos(\varphi_i) \\ \cos(\varphi_i) & \sin(\varphi_i) \end{bmatrix} \tag{13}$$

where $\boldsymbol{\xi}_i \in [-1, 1]^2$ is the location of the peak of the function, $\ell_i > 0$ is the relative length of the primary axis of the function, and $\varphi_i \in (0, \pi)$ is the orientation of the primary axis. Figure 1 shows the vorticity of the mean-reduction at base parameter values with the center of each basis function labeled. Functions f_1, f_2, and f_3 correspond to the high vorticity eddies, Functions f_4 and f_5 correspond to the low-velocity region of the flow, and Functions f_6 and f_7 correspond the main rotational flow.

To verify the BP-POD-ROM, we examine the sensitivity of 1) global kinetic energy, 2) global vorticity, and 3) local vorticities to a) Reynolds number, b) the boundary coefficient α defined in Equation (12), c) the penalty strength κ, and d) the mean-reduction defined by the location ξ, relative axis length ℓ, orientation φ_i, and maximum velocity $\bar{v}$, of each basis function in the mean-reduction. Comparing studies on flow characteristics of regularized [23] and unregularized [18] lid-driven cavities, we observe that unregularized lid-driven cavities experience vorticity closer the boundary corner behind the driving lid, top-left corner with our orientation, likely due to the higher boundary velocity in the area causing more flow into and then out of the corner. Therefore, we anticipate the flow behind the driving lid to exhibit higher sensitivity to the boundary condition and penalty, α and κ, than other locations in the domain. Additionally, we expect the method to be insensitive to mean-reduction perturbation in other areas of the domain that exhibit fewer differences between regularized and unregularized boundary conditions.

All parameters in this study were sampled uniformly except for α and κ. Instead, $\log_{10}(\alpha)$ and $\log_{10}(\kappa)$ were sampled uniformly since both parameters' effects vary on an exponential scale [12]. To quantify a range of bifurcations, we sample Reynolds number within $[11,000,\ 20,000]$ for the $Re = 17{,}000$ dataset and $[19,000,\ 28,000]$ for the $Re = 25{,}000$ dataset to check stability over large Reynolds number perturbations. Both of these ranges include both quasi-periodic and aperiodic flow, but the lower range is primarily quasi-periodic and the higher range is primarily aperiodic [17]. We sample $\log_{10}(\kappa)$ between $[-12, 2]$ to include the effect of having no boundary penalty and we sample $\log_{10}(\alpha)$ within $[-2, 0]$ since at $\alpha = 0.01$ and our discretization, the boundary velocity at the points closest to the corners is 0.99 making it nearly unregularized. We sample $\bar{v}_i$, and ℓ_i for each function within $\pm 25\%$ of their base values and sample φ_i within $[0, 2\pi]$ for each function. We sample the coordinates of the center of each basis ξ_i
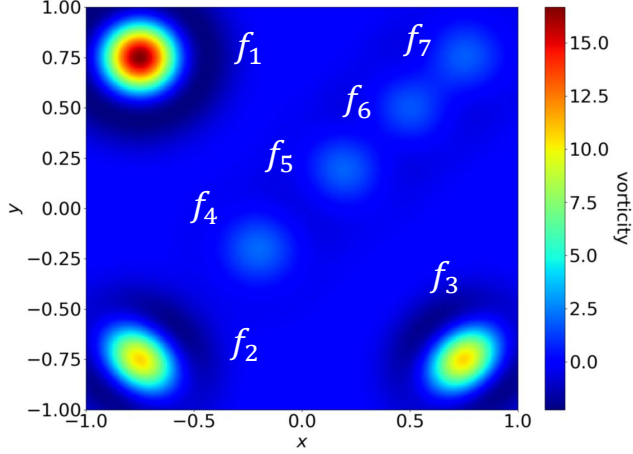
Fig. 1 Vorticity of artificial mean-reduction using Gaussian basis functions. Functions f_1, f_2, and f_3 correspond to areas of high vorticity, f_4 and f_5 to low velocity regions, and f_6 and f_7 to the main rotational flow.

within 0.2 nondimensional spatial unites of their base values. The full list of parameters with assumed base values and sampling ranges is provided in Appendix B. Note that the base values are not used in the computation of Morris indices.

To quantify the effect of parameter variations globally, we compute the kinetic energy K_E and the integrated vorticity V. We also measure the local effects of parameter variations using seven local vorticities,

$$V_i = \int_{B_i} \omega(x)dx, \quad B_i = \{x \in [-1, 1]^2 \mid \|x - \xi_i\| \leq 0.2\}, \quad i = 1, ..., 7 \tag{14}$$

where ξ_i is the base location for the ith mean-reduction function. The local vorticities allow differentiating parameter effects at characteristic locations of the flow and whether the effects of local perturbations to the mean-reduction are limited to that region. We compute sensitivities at $t = 150$, the final snapshot in the data, and at $t = 300$ to observe if any changes in sensitivities occur when solving the BP-POD-ROM for snapshots not provided by data.

III. Results and Discussion

We illustrate in Figure 2 the Morris absolute mean sensitivities for locally integrated vorticities with respect to Reynolds number, the boundary condition exponent, penalty strength, and mean-reduction parameters at Re =17,000 and Re =25,000. At both Reynolds numbers, the local vorticities, except for the high vorticity eddies V_1, V_2, and V_3, are insensitive to all parameters. The vorticity in the bottom-left is significantly more sensitive to the boundary condition and penalty strength than the vorticity in the top-left is, even though that is the region adjacent to the perturbed boundary. Additionally, the sensitivity of the third vorticity region, corresponding to the bottom-right, is significantly more sensitive at Re =25,000 than at Re =17,000. This may be due to the increased complexity of the shear layer and counterrotating corner vortex at the higher Reynolds number.

To further demonstrate differences in locally integrated vorticities, we illustrate in Figure 3 the sensitivity of the

x-velocity at each cell to the boundary condition. As anticipated, both Reynolds number cases have high sensitivities along the edge of the rotational flow, with highest sensitivity in the high-vorticity areas near the corners. However, the sensitivity in the top corners is minimal, even though this is the region of greatest difference between regularized and unregularized lid-driven cavity boundary conditions. Low-sensitivity in this region highlights a limitation of POD-ROMs that they cannot quantify dynamics that are not included in the initial POD basis and these regions are relatively stagnant in the unregularized POD basis. However, the boundary penalty still exhibits expected sensitivity in high-vorticity corners and at the edge of the rotational flow while having minimal sensitivity in other regions despite mean-reduction perturbation.

Figures 4 and 5 show the Morris screening absolute mean and standard deviation of sensitivity at $t = 150$, normalized to the maximum corresponding sensitivity index for each quantity. We restrict these plots to the sensitive parameters identified in Figure 2 and divide by the maximum sensitivity for each quantity to identify which parameter is most sensitive for each quantity. We observe that $\bar{v}_1$ is the most sensitive parameter for both $Re = 17{,}000$ and $Re = 25{,}000$, and that all quantities are insensitive to all other mean decomposition parameters. For $Re = 17{,}000$, the Reynolds number is the next most sensitive parameter and the penalty strength and boundary condition are relatively insensitive. In contrast, for $Re = 25{,}000$, all three parameters have similar sensitivities for all quantities. The mean-reduction parameters, except $\bar{v}_1$, all have low standard deviations, indicating that sensitivity of these parameters is small for all parameter combinations sampled. Additionally, $\bar{v}_1$ has the highest standard deviation of sensitivity for most quantities, suggesting that kinetic energy and vorticity may be insensitive to $\bar{v}_1$ at some parameter combinations, even though $\bar{v}_1$ is the most sensitive parameter. This is expected since $\bar{v}_1$ changes the structure of modes at the boundary, but the effect of mode structure at the boundary is highly dependent on the κ and α. For both $Re = 17{,}000$ and $Re = 25{,}000$, $\bar{v}_1$ had the largest μ^* for all quantities, but κ or α have higher σ for the kinetic energy, and the locally integrated vorticities for the high-vorticity regions. High σ for κ and α are due to coupling between the effects of the boundary penalty used and the strength with which the penalty is applied.

Figure 6 shows the Morris screening absolute mean sensitivity at $t = 300$, normalized to the maximum corresponding sensitivity index for each quantity. We note that for both Reynolds numbers, the relative sensitivity of the mean decomposition increases significantly compared to $t = 150$. However, all quantities remain more sensitive to Re, α, κ, and $\bar{v}_1$ than the other mean decomposition parameters. For $Re = 17{,}000$, we observe increases to the relative sensitivity of all quantities to most mean-reduction parameters. However, all quantities remain less sensitivity to mean-reduction parameters, with the exception of $\bar{v}_1$, than to Re, α, and κ. We observe similar increases to sensitivity for $Re = 25{,}000$, but with greater increases to sensitivity of local vorticities to mean-reduction parameters in the corners of the lid-driven cavity. We also note that for both Reynolds numbers, the relative sensitivity of all quantities Re increases but $\bar{v}_1$ is still the most sensitive parameter. These sensitivities at extrapolated times demonstrate that the ROM likely has increasing instability since the sensitivity significantly increased for mean-reduction parameters that were not sensitive at $t = 150$.

Instability for POD-ROMs in extrapolatory regimes, especially when applied to Navier-Stokes equations, is a common property [27, 28]. However, these results provide evidence that Morris screening sensitivity estimates are still reliable in these unstable cases since which parameters are the most influential is consistent between the stable $t = 150$ case and unstable $t = 300$ case.
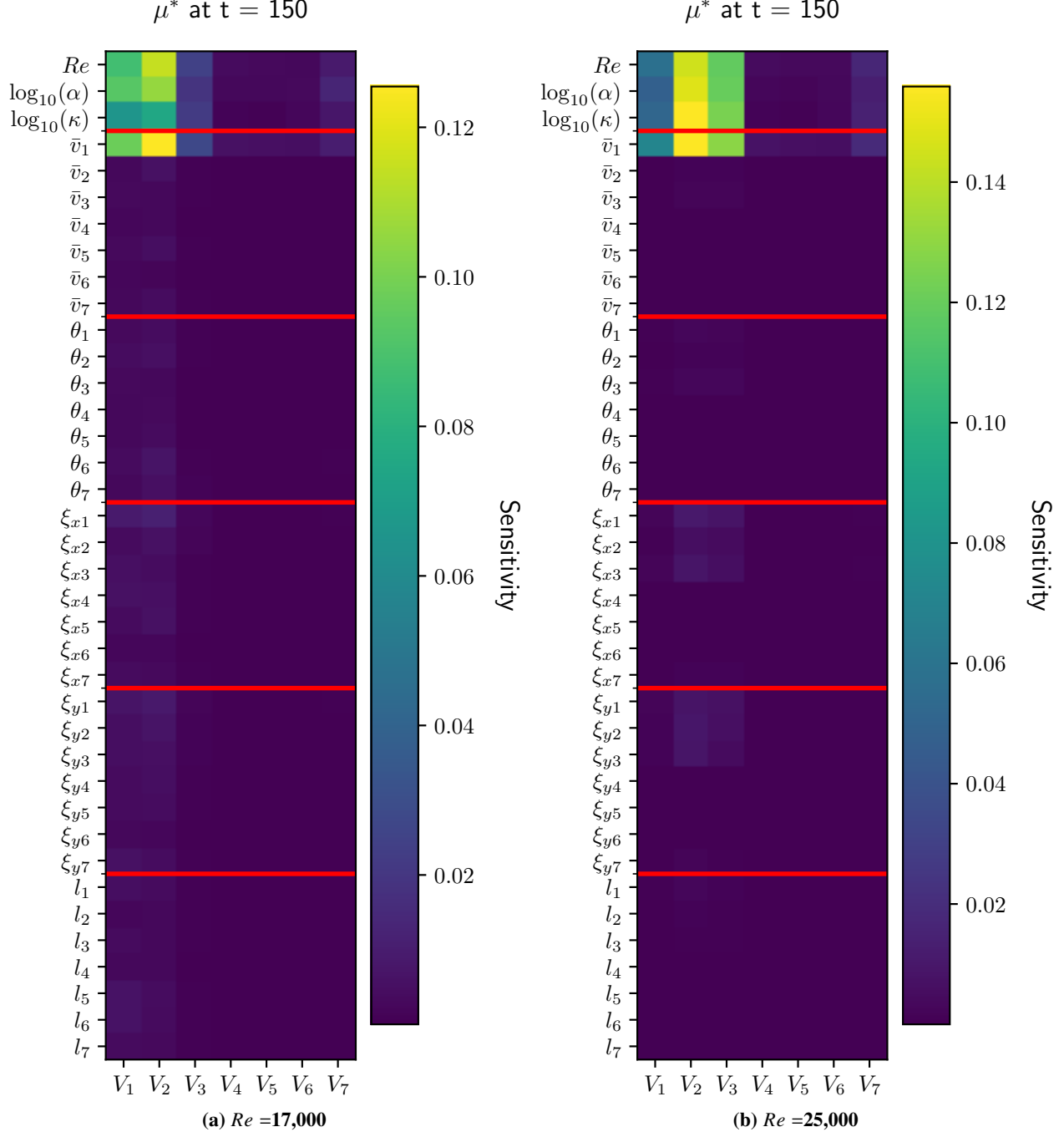

Fig. 2 **Morris mean absolute sensitivity results for local integrated vorticities at $t = 150$ and at (a) $Re =$17,000 and (b) $Re =$25,000. Each cell is μ^* for the corresponding quantity (x-axis) and parameter (y-axis).**
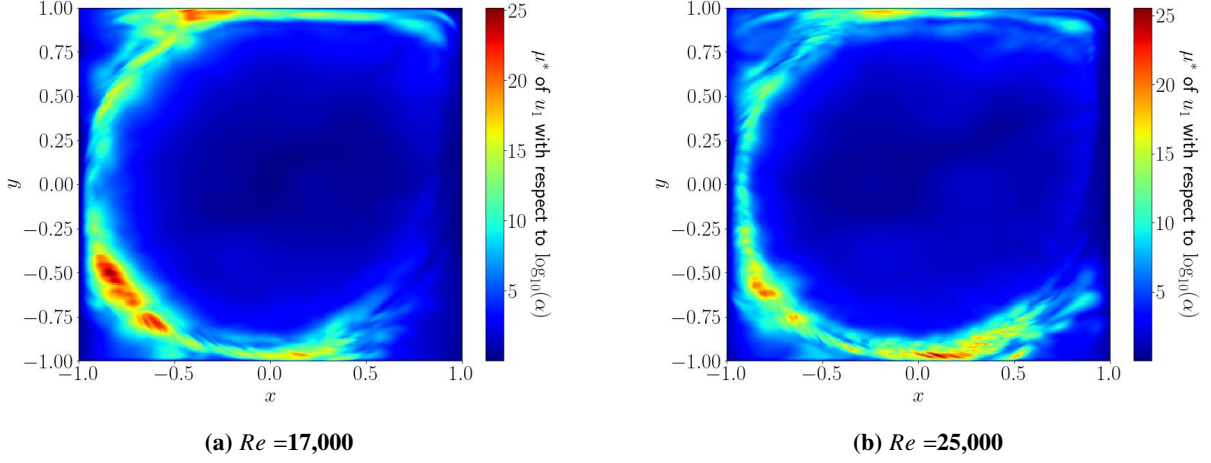
(a) *Re* =**17,000**

(b) *Re* =**25,000**

Fig. 3   Morris mean absolute sensitivity of u^x to boundary condition at (a) *Re* =**17,000 and (b)** *Re* =**25,000.**
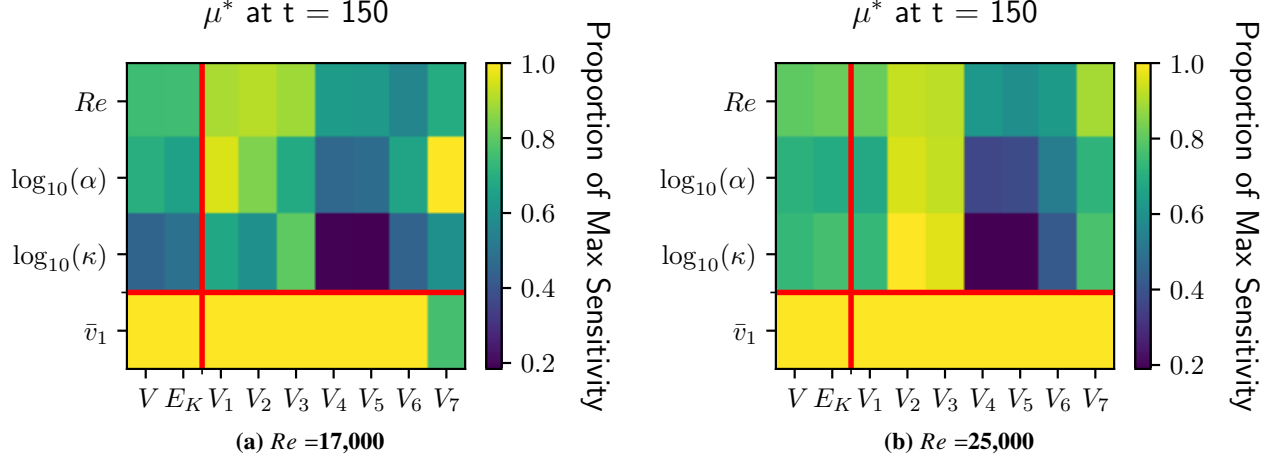
(a) *Re* =**17,000**

(b) *Re* =**25,000**

**Fig. 4   Morris mean absolute sensitivity results for global and local quantities at (a)** $Re = 17,000$ **and (b)** $Re = 25,000$. **Each cell is μ^* for the corresponding quantity (x-axis) and parameter (y-axis), divided by the maximum μ^* for that quantity.**
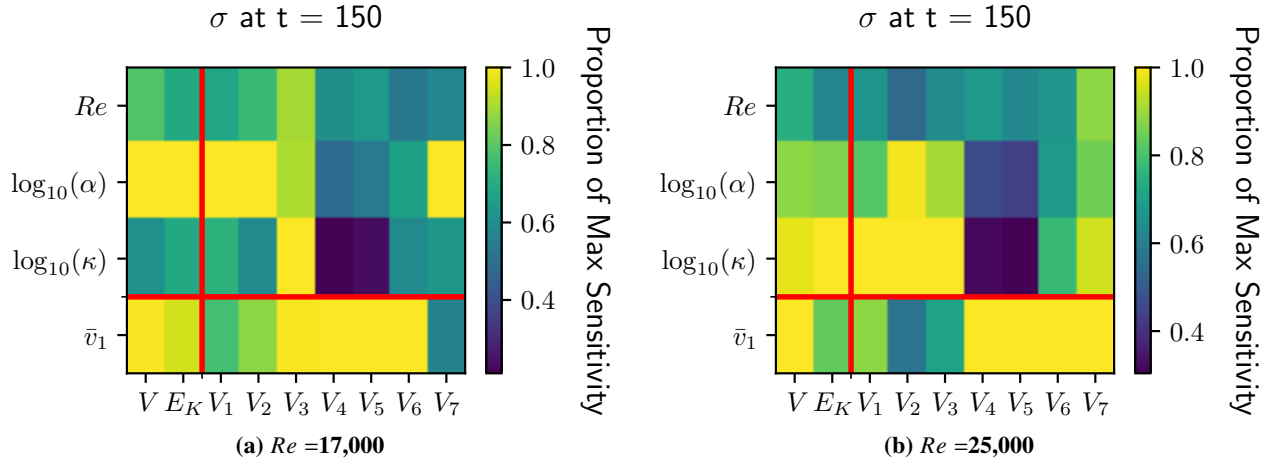

(a) *Re* =**17,000**

(b) *Re* =**25,000**

Fig. 5   Morris standard deviation of sensitivity indices for global and local quantities at (a) *Re* =**17,000 and (b)** *Re* =**25,000. Each cell is σ^* for the corresponding quantity (x-axis) and parameter (y-axis), divided by the maximum σ^* for that quantity.**

12
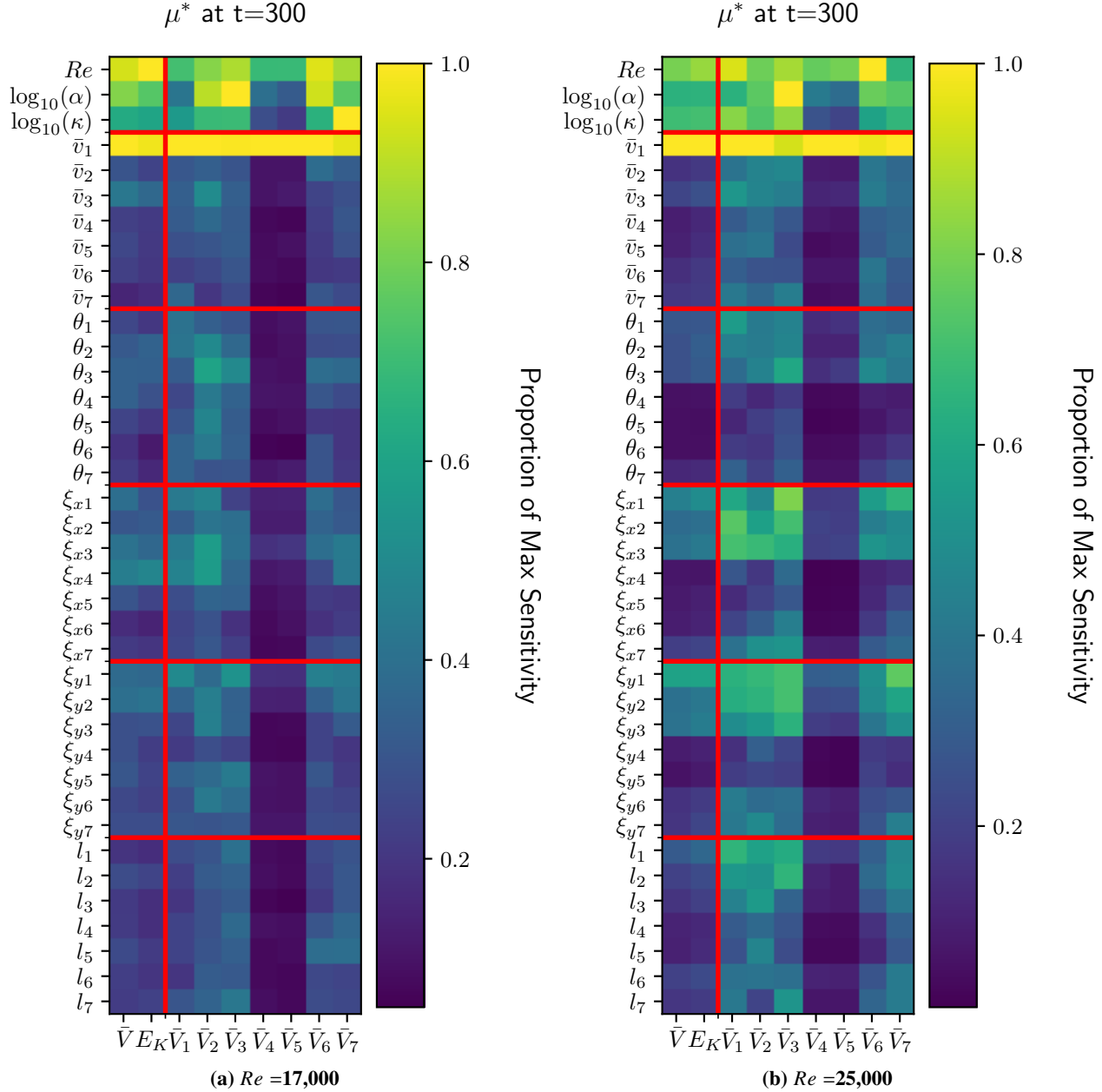
Fig. 6 Morris mean absolute sensitivity results for global and local quantities at $t = 300$ **and (a)** Re **=17,000 and (b)** Re **=25,000. Each cell is** μ^* **for the corresponding quantity (x-axis) and parameter (y-axis), divided by the maximum** μ^* **for that quantity.**

IV. Conclusions

Quantification of CFD simulation variability with respect to boundary conditions and Reynolds number is an important step to minimize risk and optimize performance for a wide variety of aerospace applications. Sensitivity analysis quantifies for which parameters variability influences model outputs. Parameter sensitivities can then be used in uncertainty quantification by identifying which parameters can be fixed without reducing model accuracy. However, high-fidelity simulations are too computationally expensive for most sensitivity analysis whereas traditional proper orthogonal decomposition-based Galerkin reduced-order models (POD-ROMs) do not permit variation of boundary conditions. We address this by using POD-ROMs with boundary penalties (BP-POD-ROM) to allow perturbation of boundary conditions, making sensitivity analysis feasible.

We tested the sensitivity of boundary conditions using a BP-POD-ROM on a lid-driven cavity test case at Re =17,000 and Re =25,000. As anticipated, a BP-POD-ROM constructed with regularized lid-driven cavity data exhibits high sensitivity to the boundary condition behind the driving lid and in the lower corner vorticity regions when perturbing towards a regularized boundary condition. This result is consistent with comparisons of flow characteristics for regularized and unregularized lid-driven cavities, which have the greatest variation between boundary conditions and Reynolds numbers in these regions [17, 18].

We determined that the kinetic energy and vorticity were most sensitive to the Reynolds number Re and the velocity of the mean-reduction in the top-left $\bar{v}_1$. The BP-POD-ROM is likely highly sensitive to the mean-reduction in the top-left since it influences the structure of POD modes at the boundary perturbations, thereby affecting the structure of modes that are strengthened and weakened by the penalty. All quantities were insensitive to the mean-reduction parameters at $t = 150$, except for the velocity in the top-left, confirming that perturbations to the mean-reduction in areas minimally affected by the boundary condition or Reynolds number do not produce vorticity. However, sensitivity to mean-reduction parameters did increase with longer time integration, likely due to model error in the extrapolatory regime. Finally, sensitivity of velocity showed that the expected high-vorticity areas were sensitive to the boundary condition but the corners with boundary discontinuities were not.

The BP-POD-ROM provides a novel approach to sensitivity analysis of CFD data. By specifying boundary conditions in a Galerkin POD-ROM, the approach allows sensitivity analysis of boundary parameters, such as surface roughness, that are too computationally intensive to study with high-fidelity simulations. For future research, we plan to extended the boundary penalty method to measure sensitivity of POD-ROM models with a larger physical parameter space such as flows through axially symmetric tanks. Models with more physical parameters permits the analysis boundary penalty sensitivity accuracy across greater basis variations, rather than the artificially perturbed basis and two Reynolds samples used here. We will also test BP-POD-ROMs parameter inference accuracy to determine whether these models can be used to accurately determine parameter values and predict uncertainty in observed quantities under boundary perturbation. These results will be critical for determining optimal implementations on larger scale CFD models.

Appendix

A. Navier-Stokes POD-ROM Matrices

Equation (15) provides the formulation of the POD-ROM matrices for the 2D incompressible Navier-Stokes with POD modes $\{\phi_m^x\}_{m=1}^M$, $\{\phi_m^y\}_{m=1}^M$ and mean reductions u_0^x, u_0^y where M is the number of POD modes. Formulations of the POD-ROM matrices were developed in Ref. [23].

$$M_{kn} = (\phi_k^i, \ \phi_n^i)_{L^2(\Omega)} \tag{15a}$$
$$= \int_\Omega \phi_k^x \phi_n^x + \phi_k^y \phi_n^y d\Omega$$

$$Q_{knm} = -(\phi_k^i, \ \phi_m^j \nabla^j \phi_n^j)_{L^2(\Omega)} \tag{15b}$$
$$= -\int_\Omega \phi_k^x \left(\phi_m^x \partial_x \phi_n^x + \phi_m^y \partial_y \phi_n^x\right) + \phi_k^y \left(\phi_m^x \partial_x \phi_n^y + \phi_m^y \partial_y \phi_n^y\right) d\Omega$$

$$L_{kn}^0 = -(\phi_k^i, u_0^j \nabla^j \phi_n^i + \phi_n^j \nabla^j u_0^i)_{L^2(\Omega)} \tag{15c}$$
$$= -\int_\Omega \phi_k^x \left(u_0^x \partial_x \phi_n^x + u_0^y \partial_y \phi_n^x + \phi_n^x \partial_x u_0^x + \phi_n^y \partial_y u_0^x\right)$$
$$+ \phi_k^y \left(u_0^x \partial_x \phi_n^y + u_0^y \partial_y \phi_n^y + \phi_n^x \partial_x u_0^y + \phi_n^y \partial_y u_0^y\right) d\Omega$$

$$Le_{kn}^{Re} = (\phi_k^i, \nabla^2 \phi_n^i)_{L^2(\Omega)} \tag{15d}$$
$$= \int_\Omega \phi_k^x(\partial_{xx} \phi_n^x + \partial_{yy} \phi_n^x) + \phi_k^y(\partial_{xx} \phi_n^y + \partial_{yy} \phi_n^y) d\Omega$$

$$Le_{kn}^{Re} = (\phi_k^i, \nabla^2 \phi_n^i)_{L^2(\Omega)} \tag{15e}$$
$$= \int_\Omega \phi_k^x(\partial_{xx} \phi_n^x + \partial_{yy} \phi_n^x) + \phi_k^y(\partial_{xx} \phi_n^y + \partial_{yy} \phi_n^y) d\Omega$$

$$C_k^0 = -(\phi_k^i, u_0^j \nabla^j u_0^i)_{L^2(\Omega)} \tag{15f}$$
$$= -\int_\Omega \phi_k^x(u^x \partial_x u_0^x + u_0^y \partial_y u_0) + \phi_k^y(u_0^x \partial_x u_0^y + u_0^y \partial_y u_0^y) d\Omega$$

$$C_k^{Re} = (\phi_k^i, \nabla^2 u_0^i)_{L^2(\Omega)} \tag{15g}$$
$$= \int_\Omega \phi_k^x(\partial_{xx} u_0^x + \partial_{yy} u_0^x) + \phi_k^y(\partial_{xx} u_0^y + \partial_{yy} u_0^y) d\Omega$$

B. Parameter Values and Sampling Ranges

Table B.1 compiles the list of model parameters, base values, and sampling ranges for sensitivity analysis. Note that base values are not used in computation of sensitivity indices and are either nominal values for the initial data or the assumed parameters for the mean-reduction displayed in Figure 1.

Table B.1 Base parameter values and sampling ranges for Morris screening.

Parameter	Base Value	Sampling Ranges
Re (17,000 Case)	17,000	[11,000, 20,000]
Re (25,000 Case)	25,000	[19,000, 28,000]
$\log_{10}(\alpha)$	0	[−2, 0]
$\log_{10}(\kappa)$	−12	[−12, 0]
ξ_{x1}	−0.75	[−0.9375, −0.5625]
ξ_{x2}	−0.75	[−0.9375, −0.5625]
ξ_{x3}	0.75	[0.5625, 0.9375]
ξ_{x4}	−0.2	[−0.25, −0.15]
ξ_{x5}	0.2	[0.15, −0.25]
ξ_{x6}	0.5	[0.375, 0.625]
ξ_{x7}	0.75	[0.5625, 0.9375]
ξ_{y1}	0.75	[0.5625, 0.9375,]
ξ_{y2}	−0.75	[−0.9375, −0.5625]
ξ_{y2}	−0.75	[−0.9375, −0.5625]
ξ_{y4}	−0.2	[−0.25, −0.15]
ξ_{y5}	0.2	[0.15, 0.25]
ξ_{y6}	0.5	[0.375, 0.625]
ξ_{y7}	0.75	[0.5625, 0.9375]

Parameter	Base Value	Sampling Ranges
$\bar{v}_1$	.95	[0.7125, 1.1875]
$\bar{v}_2$	.5	[0.375, 0.625]
$\bar{v}_3$	.5	[0.7125, 1.1875]
$\bar{v}_4$	.1	[0.075, 0.125]
$\bar{v}_5$	.1	[0.075, 0.125]
$\bar{v}_6$	.1	[0.075, 0.125]
$\bar{v}_7$	.1	[0.075, 0.125]
θ_1	0	[0, 2π]
θ_2	$\frac{3\pi}{4}$	[0, 2π]
θ_3	$\frac{\pi}{4}$	[0, 2π]
θ_4	0	[0, 2π]
θ_5	0	[0, 2π]
θ_6	0	[0, 2π]
θ_7	0	[0, 2π]
l_1	1	[.75, 1.25]
l_2	1.5	[1.125, 1.875]
l_3	1.5	[1.125, 1.875]
l_4	1	[.75, 1.25]
l_5	1	[.75, 1.25]
l_6	1	[.75, 1.25]
l_7	1	[.75, 1.25]

Acknowledgments

References

[1] Van Belleghem, M., Steeman, H.-J., Steeman, M., Janssens, A., and De Paepe, M., "Sensitivity analysis of CFD coupled non-isothermal heat and moisture modelling," *Building and Environment*, Vol. 45, No. 11, 2010, pp. 2485–2496. https://doi.org/10.1016/j.buildenv.2010.05.011.

[2] Amato, D., Hume, S., Grace, M., Roelke, E., and Mcmahon, J., "Mars EDL and Aerocapture Guidance under Dynamic

Uncertainty," *AAS/AIAA Astrodynamics Specialist Conference*, 2020, pp. 1–18.

[3] Lorenzoni, L. V., SanMartin, M., Steltzner, A., and Chen, A., "Preliminary Assessment of MSL EDL Sensitivity to Martian Environments," *2007 IEEE Aerospace Conference*, 2007, pp. 1–8. https://doi.org/10.1109/AERO.2007.352822.

[4] Pohya, A. A., Wicke, K., and Kilian, T., "Introducing variance-based global sensitivity analysis for uncertainty enabled operational and economic aircraft technology assessment," *Aerospace Science and Technology*, Vol. 122, 2022, p. 107441. https://doi.org/10.1016/j.ast.2022.107441.

[5] Balagangadhar, D., and Roy, S., "Design sensitivity analysis and optimization of steady fluid-thermal systems," *Computer Methods in Applied Mechanics and Engineering*, Vol. 190, No. 42, 2001, pp. 5465–5479. https://doi.org/10.1016/S0045-7825(01)00224-9.

[6] Smith, R. C., *Uncertainty Quantification: Theory, Implementation, and Applications, Second Edition*, Society for Industrial and Applied Mathematics, Philadelphia, PA, 2024. https://doi.org/10.1137/1.9781611977844.

[7] Morris, M. D., "Factorial Sampling Plans for Preliminary Computational Experiments," *Technometrics*, Vol. 33, No. 2, 1991, pp. 161–174. https://doi.org/10.1080/00401706.1991.10484804.

[8] Liu, Y., and Dinh, N., "Validation and uncertainty quantification for wall boiling closure relations in multiphase-CFD solver," *Nuclear Science and Engineering*, Vol. 193, No. 1-2, 2019, pp. 81–99. https://doi.org/10.48550/arXiv.1809.09184.

[9] Trentin, P. F. S., de Barros Martinez, P. H. B., dos Santos, G. B., Gasparin, E. E., and Salviano, L. O., "Screening analysis and unconstrained optimization of a small-scale vertical axis wind turbine," *Energy*, Vol. 240, 2022, p. 122782. https://doi.org/10.1016/j.energy.2021.122782.

[10] Saltelli, A., Tarantola, S., Campolongo, F., and Ratto, M., *Sensitivity Analysis in Practice: A Guide to Assessing Scientific Models*, John Wiley & Sons Ltd, West Sussex, England, 2004.

[11] Benner, P., Gugercin, S., and Willcox, K., "A Survey of Projection-Based Model Reduction Methods for Parametric Dynamical Systems," *SIAM Review*, Vol. 57, No. 4, 2015, pp. 483–531. https://doi.org/10.1137/130932715.

[12] Sirisup, S., and Karniadakis, G., "Stability and accuracy of periodic flow solutions obtained by a POD-penalty method," *Physica D: Nonlinear Phenomena*, Vol. 202, 2005, pp. 218–237. https://doi.org/10.1016/j.physd.2005.02.006.

[13] Bizon, K., and Continillo, G., "Reduced order modelling of chemical reactors with recycle by means of POD-penalty method," *Computers & Chemical Engineering*, Vol. 39, 2012, pp. 22–32. https://doi.org/10.1016/j.compchemeng.2011.10.001.

[14] Mastroddi, F., Stella, F., Cantiani, D., and Vetrano, F., "Linearized aeroelastic gust response analysis of a launch vehicle," *Journal of Spacecraft and Rockets*, Vol. 48, No. 3, 2011, pp. 420–432. https://doi.org/10.2514/1.47268.

[15] Krogstadt, P., and Antonia, R., "Surface roughness effects in turbulent boundary layers," *Experiments in Fluids*, Vol. 27, No. 5, 1999, pp. 450–460. https://doi.org/10.1007/s003480050370.

[16] Sousa, R., Poole, R., Afonso, A., Pinho, F., Oliveira, P., Morozov, A., and Alves, M., "Lid-driven cavity flow of viscoelastic liquids," *Journal of Non-Newtonian Fluid Mechanics*, Vol. 234, 2016, pp. 129–138. https://doi.org/10.1016/j.jnnfm.2016.03.001.

[17] Lee, M. W., Dowell, E. H., and Balajewicz, M. J., "A study of the regularized lid-driven cavity's progression to chaos," *Communications in Nonlinear Science and Numerical Simulation*, Vol. 71, 2019, pp. 50–72. https://doi.org/10.1016/j.cnsns.2018.11.010.

[18] Nuriev, A. N., Egorov, A. G., and Zaitseva, O. N., "Bifurcation analysis of steady-state flows in the lid-driven cavity," *Fluid Dynamics Research*, Vol. 48, No. 6, 2016. https://doi.org/10.1088/0169-5983/48/6/061405.

[19] Kucherenko, S., Rodriguez-Fernandez, M., Pantelides, C., and Shah, N., "Monte Carlo evaluation of derivative-based global sensitivity measures," *Reliability Engineering ,& System Safety*, Vol. 94, No. 7, 2009, pp. 1135–1148. https://doi.org/10.1016/j.ress.2008.05.006.

[20] Da Veiga, S., Gamboa, F., Iooss, B., and Prieur, C., *Basics and Trends in Sensitivity Analysis*, Society for Industrial and Applied Mathematics, Philadelphia, PA, 2021.

[21] Campolongo, F., Cariboni, J., and Saltelli, A., "An effective screening design for sensitivity analysis of large models," *Environmental Modelling & Software*, Vol. 22, No. 10, 2007, pp. 1509–1518. https://doi.org/10.1016/j.envsoft.2006.10.004.

[22] Lorenzi, S., Cammi, A., Luzzi, L., and Rozza, G., "POD-Galerkin method for finite volume approximation of Navier–Stokes and RANS equations," *Computer Methods in Applied Mechanics and Engineering*, Vol. 311, 2016, pp. 151–179. https://doi.org/10.1016/j.cma.2016.08.006.

[23] Lee, M. W., "On Improving the Predictable Accuracy of Reduced-order Models for Fluid Flows," Ph.D. thesis, Duke University, 2020.

[24] Shankar, P., and Deshpande, M., "Fluid mechanics in the driven cavity," *Annual review of fluid mechanics*, Vol. 32, No. 1, 2000, pp. 93–136. https://doi.org/10.1146/annurev.fluid.32.1.93.

[25] Shen, J., "Hopf bifurcation of the unsteady regularized driven cavity flow," *Journal of Computational Physics*, Vol. 95, No. 1, 1991, pp. 228–245. https://doi.org/10.1016/0021-9991(91)90261-I.

[26] Lee, M. W., "Steady State 2D Regularized Lid-Driven Cavity High-resolution Spatiotemporal Snapshots," *Mendeley Data*, Vol. 1, 2021. https://doi.org/10.17632/mbx34thp2y.1.

[27] Kalashnikova, I., and Barone, M. F., "On the stability and convergence of a Galerkin reduced order model (ROM) of compressible flow with solid wall and far-field boundary treatment," *International Journal for Numerical Methods in Engineering*, Vol. 83, No. 10, 2010, pp. 1345–1375. https://doi.org/10.1002/nme.2867.

[28] Barone, M. F., Kalashnikova, I., Segalman, D. J., and Thornquist, H. K., "Stable Galerkin reduced order models for linearized compressible flow," *Journal of Computational Physics*, Vol. 228, No. 6, 2009, pp. 1932–1946. https://doi.org/10.1016/j.jcp.2008.11.015.